PAPER • OPEN ACCESS

2D coherence imaging measurements of C^{2+} ion temperatures in the divertor of Wendelstein 7-X

View the article online for updates and enhancements.

2D coherence imaging measurements of C^{2+} ion temperatures in the divertor of Wendelstein 7-X

D. Gradic[1],[*] , **V. Perseo**[1] , **D.M. Kriete**[2] , **M. Krychowiak**[1], **R. König**[1],
Y. Feng[1], **M. Otte**[1], **T. Sunn Pedersen**[1] , **Y. Gao**[1] , **M. Jakubowski**[1] ,
G. Schlisio[1] , **F. Warmer**[1] and the W7-X Team[1],[a]

[1] Max-Planck-Institut für Plasmaphysik, Teilinstitut Greifswald, D-17491 Greifswald, Germany
[2] Department of Physics, Auburn University, Auburn, AL 36849, United States of America

E-mail: dgradic@ipp.mpg.de

CrossMark

Abstract

For the first time, 2D ion temperature values are derived from coherence imaging spectroscopy (CIS) fringe contrast measurements by taking Zeeman line broadening effects into account during the analysis procedure of a spatial-heterodyne CIS instrument. This allowed 2D images of C^{2+} ion temperatures (T_i) across the 3D-shaped island divertor of the Wendelstein 7-X stellarator. Ion temperatures ranging from 10 to 20 eV are observed for the C^{2+} impurity species in the region above the divertor targets. During the transition from the attached to the detached plasma state, the C^{2+} radiation zone moves from close to the divertor target towards the last closed flux surface. Within this radiation zone, C^{2+} temperature does not decrease significantly. Experimentally, the coherence imaging measurements were cross-calibrated at one poloidal cross-section using a high resolution Echelle spectrometer, that shared its sightlines with the coherence imaging diagnostic. The spectra demonstrated that, apart from Doppler broadening, the Zeeman effect significantly contributes to the spectral line broadening and cannot be neglected when analyzing the CIS contrast data for T_i extraction in the edge and scrape-off-layer of Wendelstein 7-X (W7-X), due to the relatively low temperatures ($T_i < 100$ eV) and high magnetic fields ($B \approx 2.5$ T).

Keywords: coherence imaging spectroscopy, SOL ion temperature, Wendelstein 7-X, Doppler line broadening, Zeeman effect

(Some figures may appear in colour only in the online journal)

1. Introduction

In the boundary of magnetic fusion experiments, the measurement of ion temperature, T_i, is less advanced than in the plasma core and rarely attempted. However, ion temperature data

is necessary for the accurate characterisation of the plasma exhaust into the divertor, since several important parameters such as the ion sound speed, ion heat transmission coefficients, the ion pressure and the sputtering rates depend on T_i [1]. It is reported that $T_i > T_e$ in the scrape-off-layer (SOL) of many devices [2], which is related to the different transport mechanisms of electrons and ions along the open magnetic field lines. Nonetheless, many theories and models for the plasma SOL assume $T_i = T_e$ due to the lack of knowledge about T_i, solely relying on electron temperature (T_e) measurements. Therefore, in particular for future, larger plasma experiments such as ITER, accurate measurements and understanding on T_i could

---

become essential for estimating the burning plasma heat load [2], which could potentially damage device components.

The scarcity of SOL ion temperature values has several reasons. In the plasma core, spectrometers are reliably used to derive T_i values via thermal Doppler broadening of atomic emission lines. Due to the high core temperatures, medium dispersion spectrometers (>0.1 nm/pix) can spectrally resolve the widely broadened line shapes. Furthermore, with constant plasma parameters over closed flux surfaces, a few dozen spectrometer sightlines are usually sufficient to measure a core T_i profile. This is more difficult in the plasma boundary, where T_i and other plasma parameters vary along the open magnetic field lines and, due to the cold particle temperatures in the SOL ($T_i \leqslant 100$ eV), ultra-high-wavelength-resolution spectrometers (dispersion <10 pm/pix) are required for resolving the neutral and ions line broadening. High-wavelength resolution spectrometers often suffer from low light-throughput and are restricted to a limited number of lines of sight (LOS). Especially in the three-dimensional magnetic island chain in the SOL of W7-X, where, depending on the magnetic configuration, the presence of 4 to 6 island structures complicates comprehensive measurements further. Thus, many sightlines or diagnostic locations in case of probes are required for satisfactory boundary characterisation. In a recent example, a retarding field analyzer (RFA) probe on a reciprocating manipulator has been used around the midplane of W7-X to measure the T_i edge profile through an island [3]. However, these measurements are locally restricted and do not provide temperatures close to the targets, where plasma parameters drastically change during detachment [4]. This is why, for the first time, 2D coherence imaging spectroscopy (CIS) measurements [5] are applied here for measuring the ion temperature distribution across the W7-X divertor target, since CIS doesn't suffer from either of these impediments.

CIS is a relatively new and powerful method [6] to measure two-dimensional images of LOS integrated plasma parameters. The development of CIS diagnostic capabilities is still ongoing in some areas, while in other areas, like flow velocity measurements, it has become a standard diagnostic technique, such as on DIII-D [7], MAST [8], W7-X [9] and is also foreseen on ITER [10]. On W7-X, the 2D particle flow velocity and ion temperature measurements are used to study the 3D island divertor SOL behaviour and to gain a better understanding of the convective particle transport by comparing the diagnostic data with synthetic data generated from full 3D EMC3-Eirene simulations [9].

In this paper, CIS C^{2+} T_i measurements are used to study the T_i distribution over the divertor targets during attached and detached conditions (reported in section 4). The primary focus is on the accurate analysis of the spatial-heterodyne CIS fringe contrast, which is, first of all, a measure of the spectral line broadening. In the relatively cold SOL and divertor region ($T_i < 100$ eV) of experiments like W7-X, several line broadening mechanisms can compete with each other: Doppler broadening, Stark broadening (primarily for hydrogen Balmer lines) and Zeeman splitting due to the confining magnetic field ($B \approx 2.5$ T). Since CIS does not measure the spectrum of a line

directly and thus cannot differentiate between several broadening mechanisms, a high wavelength resolution spectrometer is used to investigate relevant line broadening mechanisms for the C^{2+} line and to partly cross-calibrate the CIS interferometric signal. In section 2, the relevant line broadening mechanisms for the C^{2+} line are presented, followed by a description of the procedure on how to correct the CIS T_i values for Zeeman effect contributions. For a detailed description of the technical set-up of the CIS diagnostic at W7-X, the reader is referred to [5].

2. Methodology

CIS has the unique capability to obtain time-resolved LOS integrated 2D measurements (images) of key spectral line parameters emitted in plasmas ([6, 11]). It is a polarization interferometer that, in its simplest form, consists of a birefringent displacer plate sandwiched between crossed or parallel polarizers. A narrow-bandpass pre-filter isolates the spectral line of interest. Since there are no slits, polarization interferometers allow for 2D spectral imaging with much higher optical throughput than classical spectrometers. In the spatial-heterodyne set-up, the coherence information is encoded as an interference pattern modulated on the image [6] to allow single-frame 'snapshot' imaging. One such image is shown in figure 3 of this article. The key component of CIS are birefringent plates which produce an angle-dependent interferometric phase delay in the refracted light to generate approximately parallel spatial interference fringes in the image plane [6]. Along the fringes, the spatial resolution of the system is determined by the camera pixel size, while perpendicular to them, it is of the order of a fringe, corresponding to approximately 12 pixels in the W7-X CIS set-up. The high-resolution direction can be freely selected by rotating the plates and polarisers via remote control at W7-X. The CIS wavelength sensitivity depends on the plate thickness that determines the total group delay of the refracted light.

The interference pattern, S, can be described as follows:

$$S = \frac{I_0}{2} \left(1 + \zeta \cos \Phi\right), \tag{1}$$

where I_0 is the light intensity. Φ is the fringe phase, dependent on the wavelength center-of-mass of the entire spectrum within the selected filter passband. The fringe contrast, ζ, encodes the shape of the spectral line function and decreases the larger the observed line width. It is equal to the absolute value of the degree of coherence, γ, emitted within the spectral transmission window and is related to the normalised spectral intensity distribution, $g(\nu)$, via a Fourier transform [12]:

$$\zeta = |\gamma| = \left| \int g(\nu) \cdot \exp\left(2\pi i \hat{N} \frac{(\nu - \nu_0)}{\nu_0}\right) d\nu \right|, \tag{2}$$

where ν refers to the light frequency and ν_0 is the center-of-mass of the spectral multiplet or line. $\hat{N}$ is the total group delay induced by the birefringent plates. In case the entire observed spectrum solely consists of spectral lines of equal shape, one can derive plasma parameters like T_i from Doppler broadening

[13] or n_e from Stark broadening [14, 15]. This has been successfully achieved with CIS for atomic lines, which were completely dominated by either Doppler or Stark broadening only. When one broadening mechanism alone determines the spectral line shape, $g(\nu)$, equation (2) can be defined in terms of a single unknown parameter. 2D images of impurity or plasma temperatures have been derived in several devices: the WEGA stellarator-tokamak hybrid [16], the linear plasma experiment MAGPIE [17] and in a laboratory magnetosphere, RT-1 [18]. All these experiments are characterised by low plasma temperatures ($T_i < 10$ eV), low densities ($<10^{18}$ m^{-3}) and relatively small magnetic fields ($B < 0.5$ T), which is why Doppler broadening is dominant. CIS ion temperature measurements have also been made in the plasma core ($T_i > 500$ eV) of the TEXTOR tokamak ($B \approx 2.5$ T) [13], where, again, Doppler broadening was dominant for the selected impurity line. However, in the SOL of high-temperature plasma experiments, the Doppler, Stark and also the Zeeman effect can all significantly contribute to the line broadening, depending on the particle species. In the next subsection, the relevant line broadening mechanisms for a C^{2+} multiplet in W7-X are characterised with measurements of a high-resolution spectrometer. A short summary of existing definitions of ζ and how the Zeeman effect was included into the CIS analysis follows in section 2.2.

2.1. Spectral line broadening in the SOL of W7-X

In this work, a T_i analysis is performed for C^{2+}, which emits a prominent and intense atomic multiplet configuration centered around 465 nm. Carbon is the main intrinsic impurity radiator in W7-X, playing an essential role for the power and heat exhaust, especially for the transition to detachment [19]. C^{2+} radiates at electron temperatures around $T_e \approx 4$ to 10 eV [20, 21] (without considering CX contributions) and is therefore located close to the divertor targets in attached conditions. Highly resolved spectra show that, next to Doppler broadening, the Zeeman effect significantly contributes to the C^{2+} spectral line broadening in the W7-X SOL, similar as in the SOL of tokamaks [22]. This is demonstrated in figure 1, where simulations of the C^{2+} multiplet under the consideration of Doppler broadening only and both Zeeman effect and Doppler broadening in combination are shown. One representative spectrum of the C^{2+} multiplet in W7-X is shown in figure 2, which was measured with an ultra-high wavelength resolution spectrometer (dispersion of 1.2 pm/pix) to spectrally resolve the Zeeman features. Measured spectra are fitted with a multi-parametric least-squares routine by considering:

- Gaussian Doppler broadening (dependent on T_i),
- Zeeman splitting (dependent on the magnetic field strength, B, and the observation angle θ between the magnetic field vector $\vec{B}$ and the diagnostic LOS), and
- instrument broadening (roughly 15 pm).

T_i, B and the Doppler wavelength shift are free fit parameters of the routine. Stark broadening can be neglected for C^{2+} in the W7-X SOL. The routine finds very good fits with C^{2+} ion temperatures usually around $T_i \approx 10$ eV due to Doppler broadening. In figure 1, the ion temperature was kept the same

for both simulations, to demonstrate the additional effective broadening that arises from Zeeman splitting. Without a magnetic field, the shape of the C^{2+} multiplet depends on the intrinsic fine-structure splitting and consists of three major line components. In the presence of a static magnetic field, the C^{2+} multiplet is split into 19 components due to the Zeeman effect. At the measured conditions in the W7-X SOL, the effective broadening by Doppler and Zeeman splitting is comparable. Therefore, Zeeman splitting must be taken into account in the CIS contrast analysis, to avoid significantly overestimating the C^{2+} temperature.

The basis for determining the magnetic Zeeman effects is a code provided by Hey [23, 24], that is also implemented and accessible in the ADAS603 database [25]. It generates the Zeeman/Paschen–Back multiplet features for hydrogenic as well as non-hydrogenic species spectral lines, separated into π and σ polarisation components, if desired, as a function of magnetic field magnitude, B, and observation angle θ. C^{2+} Zeeman components generated with this code are indicated by vertical lines in figures 1 and 2. Thus, by fitting the Zeeman components for a measured spectrum, both B and θ can be derived in a line-integrated form and can be used, under some conditions, for localisation of the line emission along the spectroscopic sightline, further discussed in section 4.

2.2. Describing T_i in terms of measured CIS contrast, instrument characteristics and calculated Zeeman contrast

In this section, we will show how, in case of an assumed Gaussian line profile shape, the measured CIS contrast can be separated into different independent terms. They can be individually evaluated via known and measured instrument characteristics and simulated, local magnetic field effects (Zeeman splitting). The dependence of the fringe contrast, ζ, on the spectral line broadening mechanisms is extensively discussed in many CIS references ([6, 12, 14, 16, 26]). Equation (2) is the most accurate definition to analyse the measured contrast ζ, but has the disadvantage of involving the spectral line shape, $g(\nu)$, which cannot be directly measured by CIS. To derive physics quantities from ζ, assumptions about the functional form of $g(\nu)$ need to be made. Considering a Gaussian line shape, $g(\nu)$, due to Doppler broadening, a much simpler definition can be derived from equation (2) for ζ ([6, 13]):

$$\zeta_D = \exp\left(-\frac{T_i}{T_C}\right), \tag{3}$$

where

$$T_C = \frac{m_s c^2}{2k_B(\pi \hat{N})^2} \tag{4}$$

is a 'characteristic temperature' of the CIS system. m_s is the carbon ion mass. T_C depends on the chosen plate configuration that is incorporated in the total group delay

$$\hat{N} = -\left.\frac{\lambda_0}{2\pi} \frac{\partial \Phi}{\partial \lambda}\right|_{\lambda_0}. \tag{5}$$

Since an accurate value for $\hat{N}$ is necessary for the CIS temperature analysis, a wavelength scan was performed around
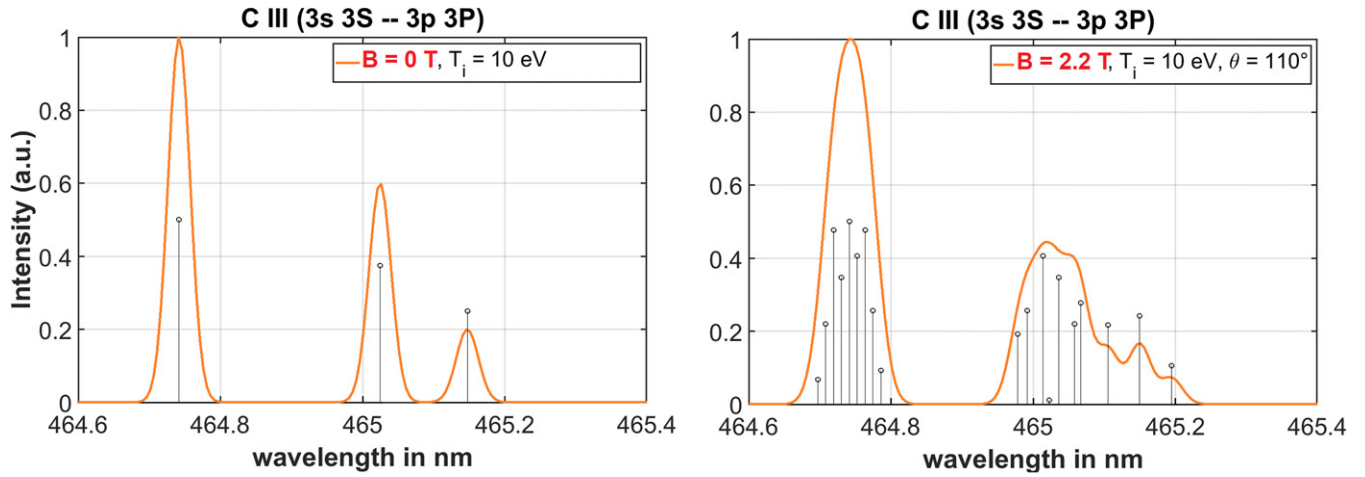
Figure 1. Simulated spectra of the C^{2+} multiplet at 464.88 nm with Doppler broadening only (left image) and with both Zeeman splitting and Doppler broadening considered (right image). Each multiplet component arising from fine-structure splitting and Zeeman splitting is indicated by a vertical line. A C^{2+} ion temperature of $T_i = 10$ eV was assumed for both simulations and, in case of additional Zeeman splitting, a magnetic field value of $B = 2.2$ T at an observation angle of $\theta = 110°$.
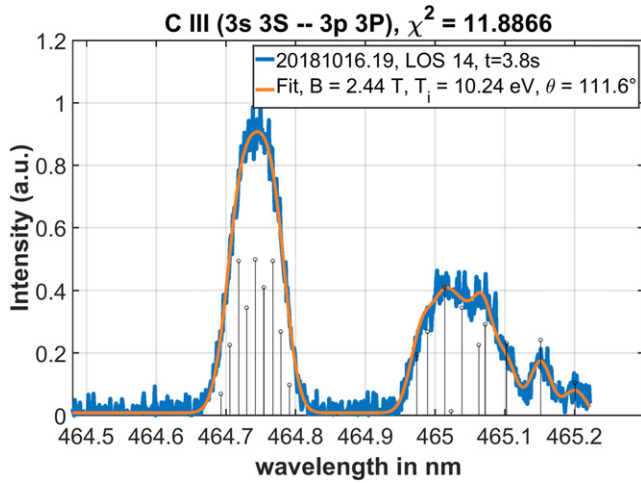

Figure 2. Measured C^{2+} line spectrum (blue) from the SOL of W7-X (along LOS 14 in figure 4) during a detached state. A spectral fit (orange) was made under the consideration of Doppler broadening, Zeeman splitting and instrument broadening of the spectrometer.

the center-of-mass frequency of the unshifted C^{2+} multiplet to measure the $\frac{\partial \Phi}{\partial \lambda}$ slope directly (documented in [5, 27]). By the fine-tuning capabilities of the calibration laser, the group delay $\hat{N}$ was accurately measured during the wavelength scan and its error is therefore small. However, equation (3) usually is not sufficient, because it neither accounts for the spectral multiplet nature of many emission lines nor for Zeeman splitting and/or Stark broadening.

If the spectrum within the interference filter transmission interval consists of the same charged state of a single species (equal Gaussian-shaped line profiles of equal width), the measured CIS contrast can be described by the product of the single Gaussian line contrast, ζ_D, and a multiplet contrast, ζ_M,

developed in [12]:

$$\zeta_M = |\gamma_M| = \left| \sum_{j=1}^{n} I_j \exp\left(2\pi i \hat{N} \frac{(\nu_j - \nu_0)}{\nu_0} \right) \right|. \quad (6)$$

This definition requires precise knowledge of the wavelength ν_j and relative intensity I_j of each single component j of the multiplet. For the evaluation of ζ_M, it is important that $\sum_{j=1}^{n} I_j = 1$. In the same way, equation (6) can also be used to accommodate for the Zeeman components. The C III 2s3d $^3P \rightarrow$ 2s3s ^3S multiplet at 464.88 nm consists of a total of 19 Zeeman components (cf figure 1). In this case, equation (6) is referred to as Zeeman contrast, ζ_{ZM}. The measured CIS contrast is then given by

$$\zeta = \zeta_D \zeta_{ZM} \zeta_{Inst}, \quad (7)$$

where ζ_{Inst} is the additional intrinsic broadening by the instrument. As for a classical spectrometer, the CIS instrument broadening can be determined with a monochromatic light source. This is routinely performed for the W7-X CIS systems during the wavelength calibration performed with a widely tuneable laser [5] before and after each W7-X plasma program. This work is based on the vertical CIS system described in [5], consisting in a 10 mm displacer plate and an additional 6 mm delay plate. This leads to a characteristic system temperature of $T_C \approx 44.6$ eV and an instrument contrast of $\zeta_{Inst} \approx 0.7$ (both vary slightly over the CIS image, due to plate imperfections, and are taken into account for the analysis). The applied plate configuration set-up was not optimised for ion temperature measurements, but for high flow velocity sensitivity.

Making use of equation (3) in equation (7), the ion temperature T_i can then be determined from the measured CIS contrast,

ζ, as follows:

$$T_{\mathrm{i}} = -T_{\mathrm{C}} \cdot \left[\ln\left(\frac{\zeta}{\zeta_{\mathrm{Inst}}}\right) - \ln\left(\zeta_{\mathrm{ZM}}\right) \right]. \qquad (8)$$

The Zeeman components can be accounted for in two complementary ways: either determining B and θ as free parameters by spectrally fitting them to experimental data from a high-resolution spectrometer, or by estimating the emission location (e.g. using the CIS intensity measurements), and then calculating B and θ at those locations, using the known coil currents and geometries of W7-X. The latter can even be corrected for finite plasma-β effects, but this was not necessary for the data presented here.

3. Evaluation of CIS contrast measurements into 2D ion temperature in the W7-X island divertor

In this article, C^{2+} ion temperature images are derived with the CIS system that had a direct view (cf figure 3) onto one of the ten island divertors of W7-X. This system allows to measure the temperature distribution above the vertical target and frontal part of the horizontal target where most of the heat and particles are exhausted in the standard magnetic configuration ([28]). Furthermore, the CIS diagnostic shared some of its sightlines with the high-resolution spectrometer (indicated by red dots in figure 3). This allows for direct, cross-diagnostic comparisons between the measured, line-integrated quantities such as intensity, temperatures or flow velocities of the observed species. The LOS of the spectrometer are shown in figure 4, collecting plasma light through a focused lens placed directly next to the CIS image bundle lens (see photo in figure 4). Both CIS and the spectrometer cover a large part of the horizontal target and the lower part of the vertical target plates, which are made of fine graphite. CIS also sees a large fraction of the baffle area, which is not intended for direct plasma contact and creates a closed-off divertor chamber.

By relaying the plasma image to the CIS camera via image guide, the original polarisation state of the Zeeman-split plasma light is not preserved when it enters the instrument. This has the advantage that the measured Zeeman spectrum does not depend on the rotation angle of the front polariser in the W7-X CIS system. However, this effect needs to be taken into account for CIS systems viewing the plasma directly through a lens without image fibres.

To evaluate 2D T_{i} values from the CIS contrast, equation (8) is applied. Both ζ_{Inst} and T_{C} are known from calibration measurements over the entire image. However, the Zeeman contrast, ζ_{ZM}, requires precise knowledge of the wavelength λ_j of each Zeeman split component and its intensity, which are determined by the local magnetic field, B, and the observation angle, θ, in the emission zone along each sightline. Both B and θ can vary considerably in a magnetic confinement device, depending on the region. Therefore, Zeeman splitting is a line-shape effect that can strongly vary over the CIS image, since B and θ are functions of space, changing the resulting line structure over the field of view or even along the sightlines if the emission zone moves.
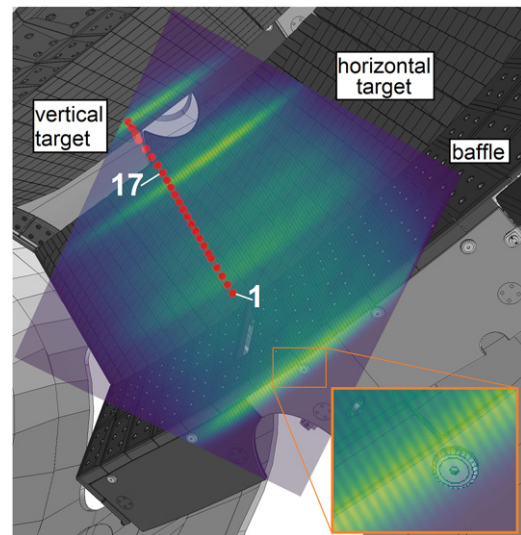

Figure 3. View of the CIS diagnostic onto one of the lower island divertors at W7-X. A CIS measurement image (indicated in blue) is transparently overlaid on top of a CAD schematic of the carbon divertor and first wall (steel). A fraction of the CIS measurement is enlarged to make the fringes of the spatial interference pattern recognisable. The CIS view was identified by objects in the camera images such as target plates or screws, which were mostly visible by reflections during the plasma dying phases. By using the coordinates of those objects, each camera pixel could be related to the coordinate system of the W7-X CAD model. The positions of the shared LOS with the spectrometer are indicated in red.

Although the CIS field of view (displayed in figure 3) is restricted to a limited region of the W7-X divertor, B and θ vary considerably. The topology of the magnetic field of W7-X is known to a very high degree of accuracy by magnetic flux surface measurements [29] and can be accessed via a field line tracer code [31]. In figure 5, the nominal values of θ at the target and wall surfaces are shown as a representative example. Across the horizontal target, the orientation angle varies by roughly $\theta \approx 30°$ in the CIS field of view. The variation of B and θ can be quantified along the shared LOS with the fits for the measured spectra by the spectrometer (such as in figure 2). Fitted values of B and θ along the shared LOS of both diagnostics are shown in figure 6 during attached conditions: B varies nearly by 0.5 T and θ by roughly 8°. Figure 7 shows the calculated ζ_{ZM} contrast for attached and detached conditions for the shared diagnostic LOS, based on the values of B and θ derived from fitting the spectra as described in section 2.1. The Zeeman contrast roughly varies between 0.2 and 0.3, which substantially decreases the measured CIS total contrast[3], ζ, according to equation (7). This can still be improved by including the Zeeman broadening effect in the optimisation of the bire-fringent plates configuration for T_{i} measurements. These plate thicknesses are different from those used in the experiments reported on here, since the present system was optimised for flow velocity measurements.

---

[3] The maximum possible value is $\zeta = 1$ for a monochromatic line (without instrument broadening) and the minimum value is $\zeta = 0$ (no interference fringes) for a quasi-continuous spectrum.
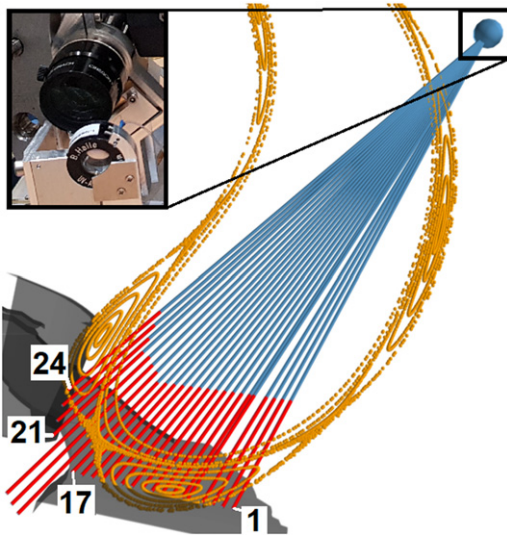
Figure 4. The 24 LOS of the spectrometer (in red and blue, red indicating the domain for B, and the observation angle, θ used for fitting the spectrometer data) onto the vertical and horizontal targets of one of the lower island divertors (transparent black). A Poincaré plot (in orange) indicates the positions of the islands in the magnetic standard configuration in vacuum. The lenses for the CIS image guide and the spectrometer fibres are photographed in the upper left corner. The end points of the spectrometer LOS on the targets were identified by back-illumination of the fibres.
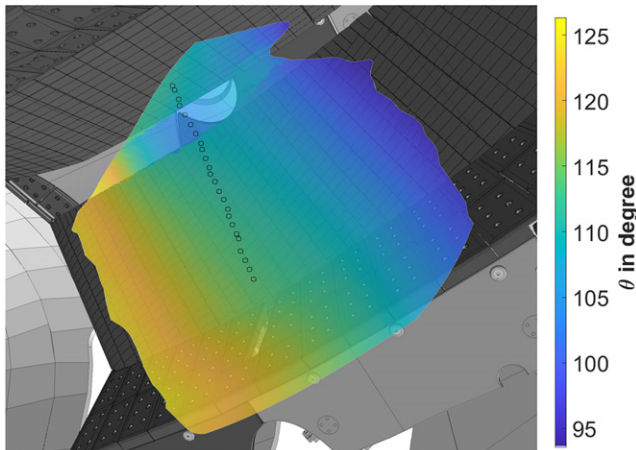

Figure 5. The variation of θ at the target and wall surfaces in the CIS field of view, displayed in the area of significant C^{2+} emission. The values are representative for the magnetic standard configuration with $B = 2.6$ T on the main magnetic axis. The positions of the shared LOS with the spectrometer are indicated with black circles.

The variation of ζ_{ZM} over the CIS field of view is significant and needs to be adequately dealt with in the T_i analysis. As example, along the shared LOS, a ζ_{ZM} variation between 0.2 and 0.3 translates into a variation of roughly 10 eV for T_i, if all other parameters for the ion temperature evaluation (cf equation (8)) are kept constant. This is on the order of the measured C^{2+} temperature derived from spectrometer measurements as in figure 2. The variation of ζ_{ZM} in the CIS image not covered by the spectrometer LOS is even larger. It is therefore necessary to determine ζ_{ZM} as accurately as is reasonably
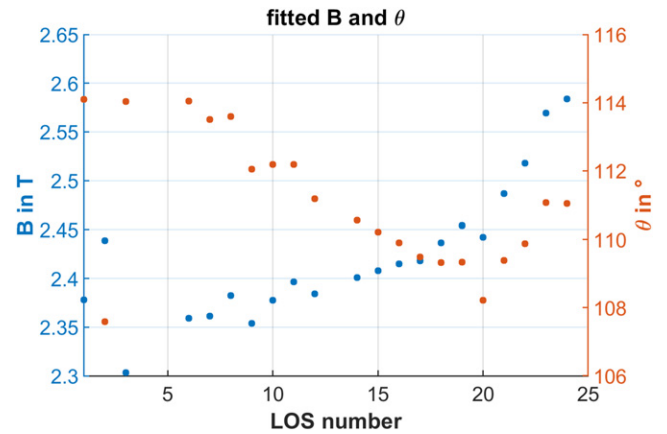

Figure 6. The fitted values of B and θ along the shared diagnostic LOS in figure 3 at $t = 2$ s during W7-X program 20181016.19.
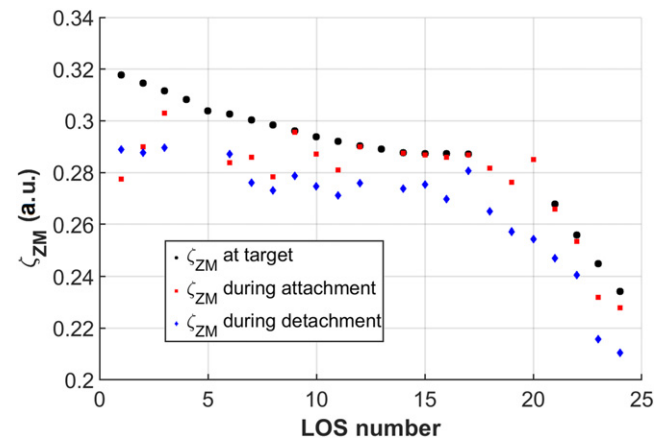

Figure 7. The values of ζ_{ZM} along the shared LOS between the spectrometer and CIS during W7-X program 20181016.19 during attached ($t = 2$ s, red squares) and detached conditions ($t = 4$ s, blue diamonds). Theoretical values for ζ_{ZM} (black dots) with the nominal B and θ values at the target surfaces have been added for comparison.

possible based on a combination of spectral fitting for each of the common LOS, with a first order approximation of the Zeeman effect on each LOS in the camera image. This means ζ_{ZM} will vary across the entire 2D image. Investigations are presently ongoing to find out whether this can be avoided by optimising the plate configuration for minimum variation of ζ_{ZM} across the entire camera view.

To analyse the ion temperature across the entire CIS view, we used ζ_{ZM} derived from the fitted B and θ values at the shared LOS. However, this does not capture the variation of B and θ further away from the spectrometer LOS. Therefore, we evaluated ζ_{ZM} with B and θ determined with the field line tracer code at the target surfaces for each camera pixel and calculated the difference in ζ_{ZM} for each pixel in relation to the closest spectrometer LOS in the image. The variation in ζ_{ZM} from this theoretical point of view was then subtracted from the fitted ζ_{ZM} in the closest LOS at each point in time. This should capture the variation of B and θ over the CIS image, also if the C^{2+} radiation front moves upwards. Figure 8 shows the ζ_{ZM}
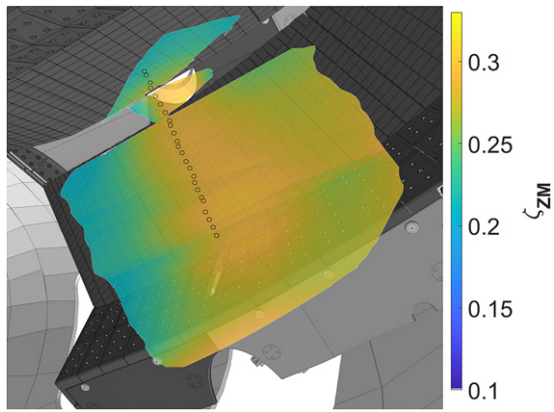
Figure 8. The variation of ζ_{ZM} over the CIS camera image at $t = 2$ s during W7-X program 20181016.19. All areas where brightness <5% of maximum intensity are greyed out. The positions of the shared LOS with the spectrometer are marked by black circles.

image evaluated by this procedure at a selected point in time. There is a considerable variation of ζ_{ZM} further away from the shared diagnostic LOS, arising from the variation of B and θ in W7-X magnetic standard configuration. ζ_{ZM} varies over time during the plasma program, depending on the fitted B and θ values measured by the spectrometer.

The derived CIS T_i values are compared with the spectrometer T_i values along two shared LOS in figure 9. Additionally, T_i was derived for CIS without the term of ζ_{ZM} in equation (8), to demonstrate the significance of the Zeeman contrast on the analysed CIS T_i values: if not considered, C^{2+} temperature would be overestimated at values around $T_i \approx 70$ to 80 eV, whereas with ζ_{ZM} considered, $T_i \approx 15$ eV, which is in good agreement with the spectrometer values.

Concerning the T_i values derived with the complete equation (8), there are discrepancies with the spectrometer T_i values for some of the shared LOS, as shown in one exemplary case in figure 9: for LOS 14, the spectrometer indicates lower T_i values by a few eV during the attached state, whereas during detachment (starting around $t = 2.4$ s) there is good agreement. Since both T_C and ζ_{Inst} are determined by extensive calibration measurements and have small errors, the T_i discrepancy is not considered to be caused by the CIS system characterization. Artificial broadening by e.g. LOS integration is the same for CIS and the spectrometer, since they measure along the same LOS. The discrepancy for LOS 14 is likely caused by a small perturbing line inside the C^{2+} multiplet, which was not included in the spectrometer fit, but is present in the CIS contrast signal (cf figure 10). It is an oxygen line also reported in other devices [23], which disappears during detachment in W7-X (as in figure 2). The oxygen line is observed for LOS 14, 22 and 23 during the attached state. The line might also be present along further LOS, but cannot be detected clearly due to the low signal-to-noise ratio of the spectrometer. Along other LOS (e.g. LOS 6–8), the agreement is good for the entire plasma duration, also in attached state, because no perturbing lines are present. Further causes for discrepancies between the two diagnostics might be different focus settings of the diagnostics, a possible, slight mismatch

of the shared LOS onto the pumping gap and vertical target and background emission due to bremsstrahlung and thermal emission. Spectral background is deducted from the fits, but not accounted for in the CIS contrast analysis. The spectral background contributes over the entire range of the narrowbandpass CIS filter (≈ 2 nm) to the measured CIS contrast, ζ. The influence of continuous background emission on the CIS contrast is currently being investigated and will be published in a future publication.

4. Ion temperature distribution across the W7-X island divertor during attached and detached plasma operation phases

In this section, the T_i results for the C^{2+} multiplet in the W7-X island divertor are presented. The T_i analysis was performed according to equation (8), where the Zeeman contrast ζ_{ZM} is evaluated with the procedure explained in the previous section. A W7-X program with a transition into detachment was selected for the T_i analysis, to investigate the evolution of T_i between attached and detached conditions. Figure 11 shows the time traces of the selected program. Detachment with $f_{rad} \approx 0.8$ is achieved by hydrogen fueling through the divertor gas inlet system [32] in one of the island divertors. The transition into detachment starts around $t = 2.4$ s and then the plasma stays detached, also after an unplanned decrease of ECRH power at $t = 3$ s, caused by a drop-out of some gyrotrons. Due to the sudden drop of core electron temperature, the divertor gas valve was automatically closed, reducing the density. Detachment was sustained, because at less ECRH power, less edge electron density is required for accessing the detached state in W7-X. Two time points were selected for the CIS analysis at $t = 2$ s (attached state) and $t = 4$ s (detached state).

C^{2+} brightness and T_i image results are shown in figures 12 and 13. Additionally, the corresponding localisation results of the C^{2+} emission, obtained by spectral fitting of the high-resolution spectrometer measurements, can be seen in figure 14. In attached conditions, values of $T_i \approx 10$ to 20 eV are observed in the divertor areas, with the C^{2+} emission located close to the targets. Interestingly, two line-shaped areas of increased ion temperatures $T_i \approx 20$ eV are present between LOS 13 and 18 in the attached state T_i image. These lines are in the proximity of the strike-line along the horizontal target, close to the pumping gap, where a maximum in the C^{2+} emission is also observed in the brightness image at $t = 2$ s. The two line-shaped areas with higher T_i values disappear after the transition to detachment, where a drop in T_i is measured by CIS and the C^{2+} emission has moved towards the lastclosed flux surface (LCFS), according to localisation results in figure 14. Such a shift in C^{2+} emission is seen experimentally [4, 30] as well as in EMC3-Eirene simulations performed for different magnetic configurations at different radiated power fractions, as exemplified in figure 15. A profound movement for C^{2+} in particular is reported as well in radiated power studies during detachment in the tokamak DIII-D [21]. Along other areas above the horizontal target, however, T_i stays more or less constant.
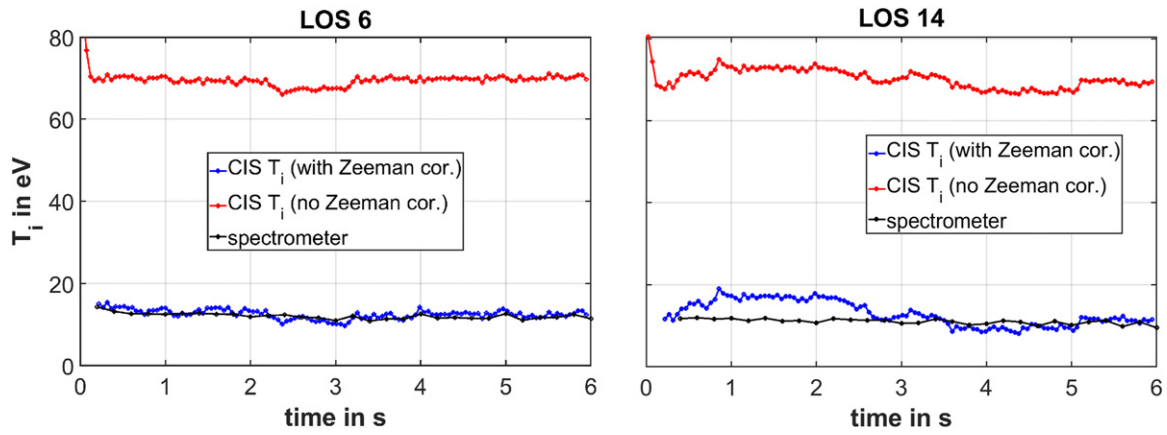
Figure 9. Comparison of T_i values derived with the spectrometer (black) and the CIS (blue and red) for the shared LOS numbers 6 and 14 during W7-X program 20181016.19.
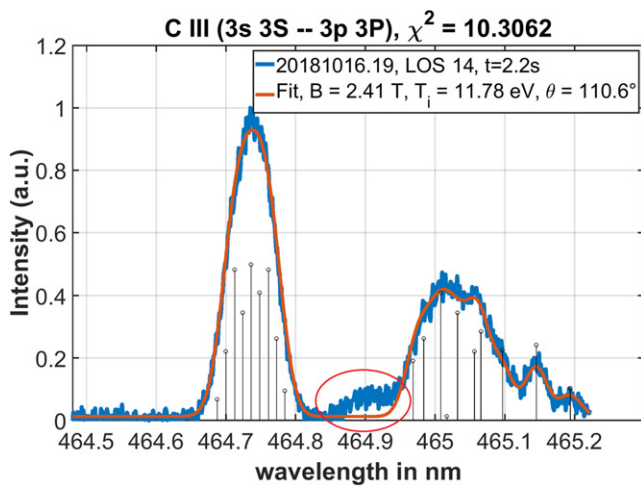

Figure 10. Measured C^{2+} line spectrum (blue) from the SOL of W7-X (along LOS 14 in figure 4) during attached conditions. A spectral fit (orange) was made under the consideration of Doppler broadening, Zeeman splitting and instrument broadening of the spectrometer. A perturbing line in the C^{2+} multiplet is indicated by a red frame.

It is assumed that the two line-shaped areas of increased T_i values between LOS 13 and 18 are artificially caused by a perturbing oxygen line in the C^{2+} multiplet along these LOS, indicated in figure 10. The oxygen line disappears after the transition into detachment, according to the spectrometer measurements. Due to the proximity to the plasma exhaust strike-line on the target, the perturbing line could be the result of oxygen atoms being released from the target structures due to plasma-wall interactions and/or locally higher target temperatures. The oxygen content decreases after the transition to detachment, when the total power load on the divertor targets is reduced. T_i values by the spectrometer are regarded as more accurate, since they better account for the background and partly also for perturbing line effects. Nonetheless, CIS T_i images provide higher spatial and temporal resolution, as demonstrated in figures 9 and 16.

In figure 13, the area beyond LOS 1 shows unexpectedly high temperatures of $T_i \approx 25$ eV, surrounding the cut-out in

the outer, low-field side baffle and even more so along the top corner of the baffle in this region. From the CIS camera viewpoint, these measurements are from regions above the baffle and might be dominated by C^{2+} emission distributed along an entire island over long integration paths (cf figure 4, where a Poincaré plot of the magnetic field topology is provided for the entire poloidal cross-section). Furthermore, some structures of the baffle tiles are recognizable in the emission and T_i images, which is a sign for reflections, although the W7-X divertor and baffle plates are made of graphite. Reflections and long line-integration paths with varying temperatures and flow velocities might lead to 'artificial' spectral line broadening, which could explain higher T_i values in this part of the CIS image. From the horizontal and vertical divertor targets, no obvious reflections could be recognized. Concerning long integration paths, this could be investigated by synthetic C^{2+} brightness and T_i images computed with the edge simulation code EMC3-Eirene, which are foreseen in the future.

The localisation of the C^{2+} emission along the spectrometer LOS, shown in figure 14, were obtained from the spectral fitting of the Zeeman components measured with the spectrometer. Interpretation of spectroscopically measured ion temperatures is difficult if the line-integrated emission cannot be localised along the LOS. In a stellarator such as W7-X, the fitted values for B and θ, which the Zeeman splitting depends on, can be used to localise the emission zone along the LOS. The vacuum magnetic field topology and strength are known to a very high degree of accuracy [29] from magnetic flux surface measurements. Localisation based on the fit values B and θ can become inaccurate if

(a) finite plasma-β effects change the magnetic field topology or

(b) strong plasma currents develop that also change the magnetic field topology or

(c) a species emits light in several regions along the LOS.

Finite-β effects can be neglected for the plasmas that have been created so far in W7-X. They could, however, be present and considered in future W7-X plasma campaigns. Concerning the second point, toroidal plasma currents in W7-X are usually
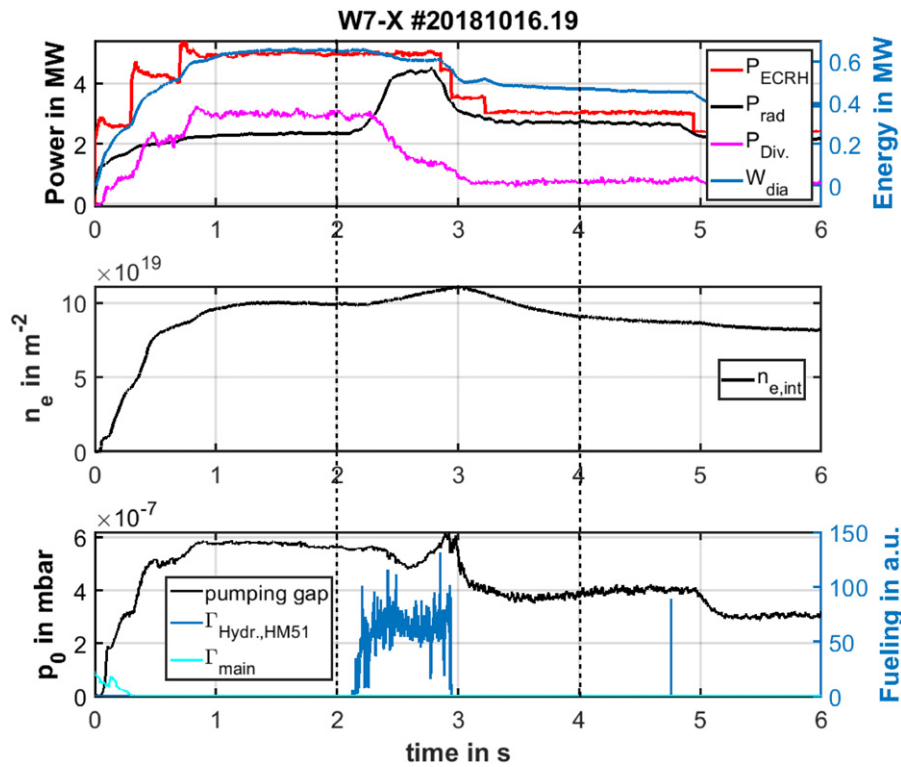
Figure 11. Data for W7-X program 20181016.19 performed in the standard magnetic configuration ($I_{cc} = 1$ kA). From top to bottom: input power and radiated power, total power load on all 10 divertors, diamagnetic energy, line integrated (core) density, neutral pressure in the pumping gap (AEI30) and seeded hydrogen gas fueling. A detachment state was induced around $t = 2.4$ s by a feedback-controlled hydrogen density ramp through the divertor gas inlet system ($\Gamma_{\mathrm{Hydr.,HM51}}$) in half module 51. Overall, the plasma duration was 20 s, but only the first 6 s are looked into for this study, because no major changes happen after $t = 5$ s.
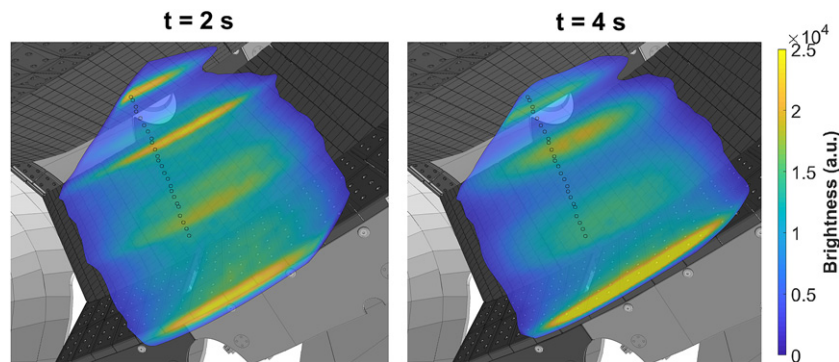

Figure 12. C^{2+} brightness images measured by CIS during attached (left) and detached (right) conditions during W7-X program 20181016.19. The black circles indicate the LOS shared with the spectrometer. The top circle represents LOS 24, the bottom one on the vertical target is LOS 1.

on the order of ± 10 kA. These currents, located in the vicinity of the magnetic axis, induce changes to the magnetic field at the boundary by about $\Delta B \leqslant 1$ mT and $\Delta \theta \leqslant 0.01°$ along the spectrometer LOS [33]. Thus, they are still well below the fitting accuracy of the spectrometer (0.1 T and 1°), and should not affect the fit results.

For the spectrometer LOS, the third point is an issue since impurity radiation does not only occur in the divertor area, but also at the edge of the magnetic island close to the window where the observation lenses are located (cf figure 4). This leads to a systematic error for the localisation by Zeeman fitting, which will be more characterised investigated with synthetic spectra in a separate publication. Especially during detachment, EMC3-Eirene simulations indicate a radiation belt around the entire LCFS [19]. During attachment, filtered camera data show C^{2+} radiation usually dominant in the divertor area close to the pumping gap, and much less intense in the islands [34].

In this publication, the method of localization by Zeeman splitting is applied to qualitatively investigate the overall movement of the C^{2+} radiation zone. The fitted localisation positions in figure 14 are expected to have a systematic
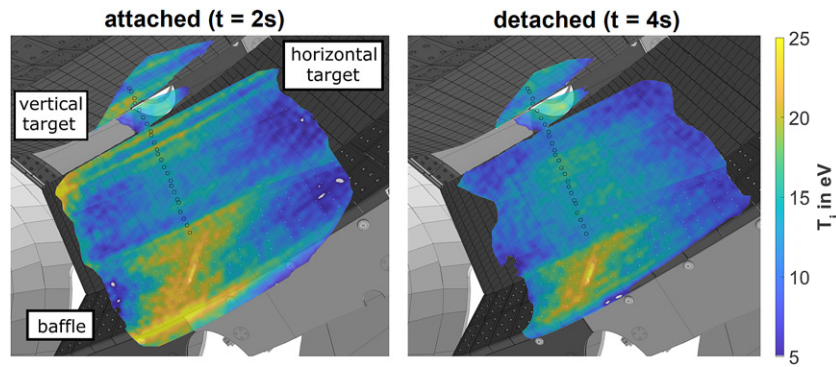
Figure 13. C^{2+} ion temperature images measured by CIS during attached and detached conditions during W7-X program 20181016.19. The black circles indicate the LOS shared with the spectrometer. The top circle represents LOS 24, the bottom one on the vertical target is LOS 1.
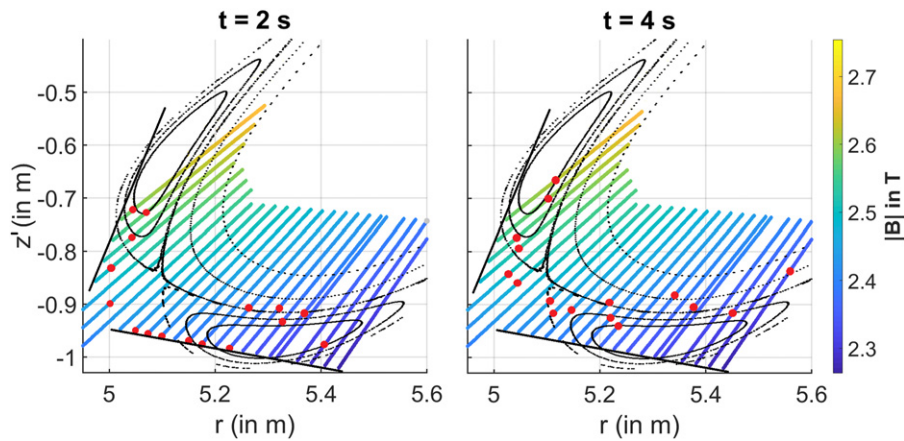

Figure 14. Localisation (red dots) of the C^{2+} emission along the 24 spectrometer LOS during attached and detached conditions in the program 20181016.19. The localisation positions have a placement error of a few centimetres. The vertical and horizontal targets are indicated by black lines and a Poincaré plot of the field lines for the magnetic island topology is also indicated in black. The magnetic field values are obtained from the field line tracer code [31] and plotted along a fraction of the LOS (marked in red in figure 4).
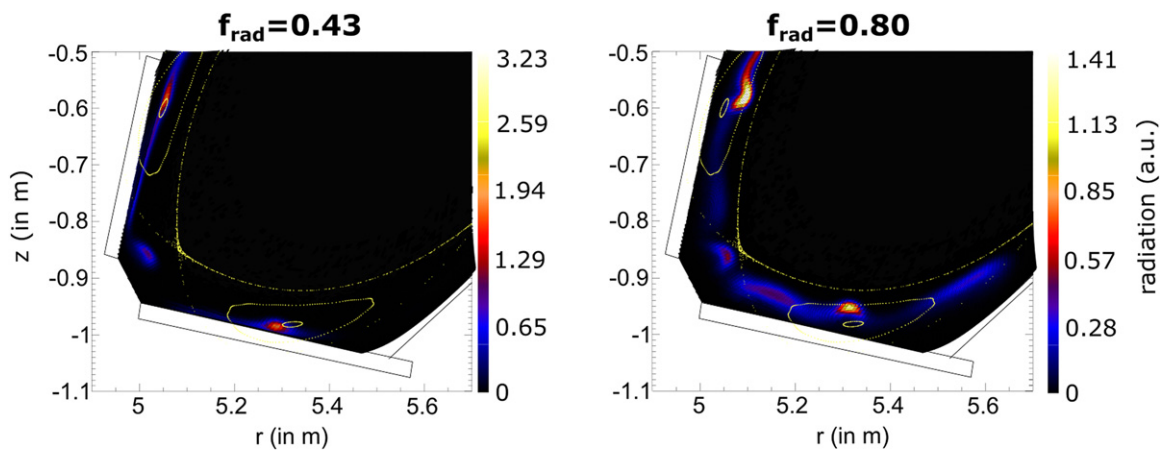

Figure 15. EMC3-Eirene simulation of the C^{2+} radiation during attached ($f_{\rm rad} \approx 0.43$) and detached ($f_{\rm rad} \approx 0.8$) states in the magnetic standard configuration without the island control coils. The simulation results are shown at the toroidal angle of $\phi = 12.3°$ for the S1 case in [19]. A Poincaré plot of the field lines for the magnetic island topology is indicated in yellow. The poloidal distribution of lowly ionized carbon can be affected by finite island control coil currents and by error fields and drift effects.

error of a few centimetres in the detached case, due to the discussed point (c). However, the overall movement of the C^{2+} radiation towards the LCFS during detachment is also confirmed by tomographic reconstructions [30] as well as
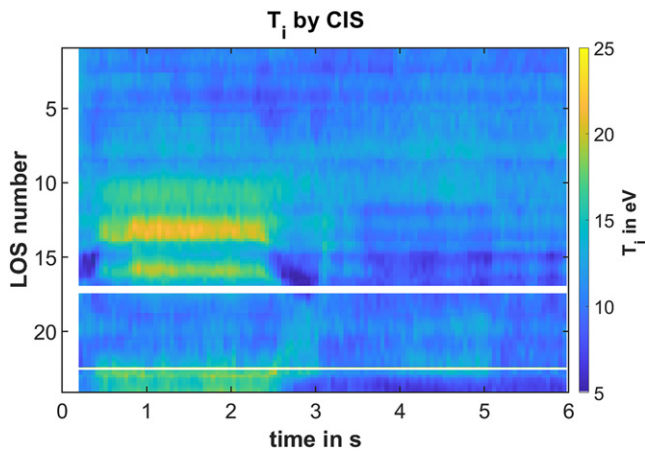
Figure 16. Temporal evolution of the analysed CIS T_i signal between LOS 1 and 24 (cf figure 13) during the first 6 s of the W7-X program 20181016.19. T_i values between LOS 13 and 18 are overestimated by a few eV predominantly due to a perturbing oxygen line in the C^{2+} multiplet, not accounted for in the CIS analysis. The spatial resolution was increased by selecting 122 points between the shared LOS 1 and 24 with Sopra. At $t = 2.4$ s, a transition into detachment occurs.

EMC3-Eirene simulations (cf figure 15). This is a general numerical result, insensitive to the details of magnetic configuration [19]. Since both CIS and spectrometer measurements are bound to the regions where C^{2+} radiates, the detection region of both diagnostics in the SOL changes during the transition from attached to detached states.

5. Summary and conclusions

At W7-X, it has been demonstrated that 2D CIS can be used not only to measure 2D flow velocity [9], but also 2D C^{2+} ion temperature distributions in the SOL, across a 3D shaped island divertor plasma. The method to derive ion temperatures from CIS contrast measurements, described in section 2.2, is based on a comparison with high spectral resolution, multi-channel Echelle spectrometer measurements at one selected cross-section of the 2D image. The measured spectra demonstrate that both Doppler broadening and Zeeman splitting need to be taken into account for the line broadening analysis. CIS suffers from the variation of the magnetic field value B and the observation angle θ across camera view, resulting in a significant variation of the Zeeman contrast over the entire image. To account for the variation of B and θ not covered by the spectrometer LOS, vacuum magnetic field data, which is provided by the field line tracer code, had to be included in the contrast analysis for the entire CIS image analysis.

This clearly emphasizes the necessity of optimising the CIS plate configuration for ion temperature measurements in the SOL of W7-X and similar devices. In order to analyse the CIS contrast signal without supporting spectrometer measurements, a first step would be to minimise the dependence of the CIS contrast on the varying Zeeman components. This is presently being investigated within our group for the next experimental campaign. New results ([15]), published very recently, propose the use of a pixelated phase mask method

of interferometry, which could be helpful in this regard. If the effect of the Zeeman contrast could be sufficiently reduced across the given field of view, a single estimate of both B and θ might become acceptable for evaluating the Zeeman contrast of the entire CIS image.

The CIS set-up analysed in this work was not optimized for temperature but flow measurements only. Therefore, a cross-validation was necessary to achieve confidence in CIS T_i results based on contrast in the interference patterns. A high-resolution spectrometer sharing several LOS with CIS was used for this purpose. Furthermore, the comparison of CIS and spectrometer T_i values revealed a discrepancy in C^{2+} ion temperature for some of the sheared LOS: CIS had higher values by a few eV. This could be explained by a perturbing oxygen line in the C^{2+} multiplet artificially increased the derived CIS T_i values. Since the perturbing line is spectrally within the C^{2+} multiplet, it cannot be avoided by choosing a different spectral range for the narrow-bandpass transmission filter. It remains to be investigated whether perturbing spectral lines can be accounted for in the CIS contrast analysis procedure by additional terms in equations (8) or (7). In addition, background radiation such as bremsstrahlung or thermal radiation from the target areas leads to a decrease of the CIS contrast and thus an artificial increase of the deduced ion temperature, T_i, by a few eV. This could be considered in future CIS analysis with additional terms in equation (8), which is currently under development. Bremsstrahlung profile measurements as well as spatially highly resolved infrared target surface temperature measurements are available and could be used to estimate the background radiation, which varies over the CIS field of view for each camera pixel. However, it is currently not clear how these effects can be sufficiently characterized without a spectrometer sharing some LOS with CIS.

Concerning SOL physics, interpretation of the CIS ion temperature images is not trivial in varying conditions, since the measurement location changes. During a transition into detachment, the emission location of the observed C^{2+} impurity species moves upstream, according to EMC3-Eirene simulations and Zeeman fitting performed on highly resolved spectra. The movement of the C^{2+} radiation zone away from the divertor targets is consistent with a drop in plasma temperature at the divertor target. Collisional radiative models predict the C^{2+} radiation to be most intense for electron temperatures in the range from $T_e \approx 4$ to 10 eV (i.e. confer figure 1 in [20]), depending on the electron density and involved collision processes. Within the receding C^{2+} layer, only a slight drop of C^{2+} ion temperature is measured. In a small region around the strike line on the horizontal target, T_i seems to decrease by a factor of 2. This apparent temperature change, however, is attributed to a perturbing impurity line within the transmission bandwidth of the narrow-bandpass interference filter used in the CIS system. The reduced target heat load caused by the transition into detachment results in the oxygen source becoming negligible and the perturbing line no longer being detectable. This suggests that the C^{2+} temperature does not significantly decrease during detachment and stays rather constant around $T_i \approx 10$ to 15 eV. Whether the ion temperature is actually higher than the electron temperature at the observed
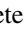
locations in the divertor region remains an open issue. Interestingly, RFA probe measurements indicate $T_i > T_e$ [3] further upstream.

Altogether, it remains an exercise to find out where exactly each atomic line radiates in the SOL. The global shift of the C^{2+} emission zone prevents the T_i measurements by spectral means at the same position close to the targets for both attached and detached scenarios. This needs to be investigated using for other impurity species, that radiate at different locations in the SOL, in the future.

Acknowledgments

ORCID iDs

D. Gradic ⓘ https://orcid.org/0000-0002-6109-9345
V. Perseo ⓘ https://orcid.org/0000-0001-8473-9002
D.M. Kriete ⓘ https://orcid.org/0000-0002-3657-2911
T. Sunn Pedersen ⓘ https://orcid.org/0000-0002-9720-1276
Y. Gao ⓘ https://orcid.org/0000-0001-8576-0970
M. Jakubowski ⓘ https://orcid.org/0000-0002-6557-3497
G. Schlisio ⓘ https://orcid.org/0000-0002-5430-0645
F. Warmer ⓘ https://orcid.org/0000-0001-9585-5201

References

[1] Stangeby P.C. 2000 *The Plasma Boundary of Magnetic Fusion Devices* (Bristol: Institute of Physics Publishing)
[2] Kocan M. *et al* 2011 Measurements of ion energies in the tokamak plasma boundary *J. Nucl. Mater.* **415** S1133–8
[3] Li Y. *et al* 2019 Measurement of the edge ion temperature in W7-X with island divertor by a retarding field analyzer probe *Nucl. Fusion* **59** 126002
[4] Schmitz O. *et al* 2021 Stable heat and particle flux detachment with efficient particle exhaust in the island divertor of Wendelstein 7-X *Nucl. Fusion* **61** 016026
[5] Perseo V., Gradic D., König R., Ford O.P., Killer C., Grulke O. and Ennis D.A. 2020 Coherence imaging spectroscopy at Wendelstein 7-X for impurity flow measurements *Rev. Sci. Instrum.* **91** 013501
[6] Howard J. 2010 Coherence imaging spectro-polarimetry for magnetic fusion diagnostics *J. Phys. B: At. Mol. Opt. Phys.* **43** 144010
[7] Howard J. *et al* 2011 Coherence imaging of flows in the DIII-D divertor *Contrib. Plasma Phys.* **51** 194–200
[8] Silburn S.A., Harrison J.R., Howard J., Gibson K.J., Meyer H., Michael C.A. and Sharples R.M. 2014 Coherence imaging of scrape-off-layer and divertor impurity flows in the Mega Amp Spherical Tokamak (invited) *Rev. Sci. Instrum.* **85** 11D703
[9] Perseo V., Effenberg F., Gradic D., König R., Ford O.P., Reimold F., Ennis D.A., Schmitz O. and Sunn Pedersen T. 2019 Direct measurements of counter-streaming flows in a low-shear stellarator magnetic island topology *Nucl. Fusion* **59** 124003
[10] Howard J., Kocan M., Lisgo S. and Reichle R. 2016 Stokes–Doppler coherence imaging for ITER boundary tomography *Rev. Sci. Instrum.* **87** 11E561
[11] Howard J., Michael C., Glass F. and Danielsson A. 2003 Time-resolved two-dimensional plasma spectroscopy using coherence-imaging techniques *Plasma Phys. Control. Fusion* **45** 1143
[12] Silburn S.A. 2014 A Doppler coherence imaging diagnostic for the Mega-Amp Spherical Tokamak University of Durham *PhD Thesis*
[13] Howard J., Jaspers R., Lischtschenko O., Delabie E. and Chung J. 2010 Imaging charge exchange recombination spectroscopy on the TEXTOR tokamak *Plasma Phys. Control. Fusion* **52** 125002
[14] Lischtschenko O., Bystrov K., De Temmerman G., Howard J., Jaspers R.J.E. and König R. 2010 Density measurements using coherence imaging spectroscopy based on Stark broadening *Rev. Sci. Instrum.* **81** 10E521
[15] Allcock J.S., Silburn S.A., Sharples R.M., Harrison J.R., Conway N.J. and Vernimmen J.W.M. 2021 2D measurements of plasma electron density using coherence imaging with a pixelated phase mask *Rev. Sci. Instrum.* **92** 073506
[16] Chung J., König R., Howard J., Otte M. and Klinger T. 2005 Time resolved coherence-imaging spectrometer on WEGA stellarator *Plasma Phys. Control. Fusion* **47** 919–40
[17] Lester R., Zhai Y., Corr C. and Howard J. 2016 Coherence imaging for ion temperature and flow measurements in a low-temperature helicon plasma source *Plasma Sources Sci. Technol.* **25** 015025
[18] Nakamura K., Nishiura M., Takahashi N., Yoshida Z., Kenmochi N., Sugata T., Katsura S. and Howard J. 2018 Coherence-imaging spectroscopy for 2D distribution of ion temperature and flow velocity in a laboratory magnetosphere *Rev. Sci. Instrum.* **89** 10D133
[19] Feng Y. *et al* ((W7-X team) 2021 Understanding detachment of the W7-X island divertor *Nucl. Fusion* **61** 086012
[20] Colgan J., Fontes C.J. and Abdallah J. Jr 2006 Collisional-radiative studies of carbon plasmas *High Energy Density Phys.* **2** 90–6
[21] Samuell C. *et al* 2021 Advancements in understanding the 2D role of impurity radiation for dissipative divertor operation on DIII-D *2020 IAEA Fusion Energy Conf.* (Virtual Event, May 2021) (https://conferences.iaea.org/event/214/papers/17149/files/6765-iaea2020_Manuscript_SamuellMcLean_v6.pdf)
[22] Hey J.D., Chu C.C. and Mertens P. 2002 Zeeman spectroscopy as a tool for studying atomic processes in edge plasmas *Contrib. Plasma Phys.* **42** 635–44
[23] Hey J.D., Chu C.C., Brezinsek S., Mertens P. and Unterberg B. 2002 Oxygen ion impurity in the TEXTOR tokamak boundary plasma observed and analysed by Zeeman spectroscopy *J. Phys. B: At. Mol. Opt. Phys.* **35** 1525–53
[24] Hey J.D., Chu C.C., Mertens P., Brezinsek S. and Unterberg B. 2004 Atomic collision processes with ions at the edge of magnetically confined fusion plasmas *J. Phys. B: At. Mol. Opt. Phys.* **37** 2543–67
[25] Summers H. 2004 The ADAS User Manual (Version 2.6) (http://adas.ac.uk)
[26] Michael C.A. 2003 Doppler spectroscopy of argon plasmas in H-1NF using a coherence imaging camera *PhD Thesis* Australian National University

[27] Gradic D., Perseo V., König R. and Ennis D. 2019 A new calibration implementation for Doppler coherence imaging spectroscopy *Fusion Eng. Des.* **146** 995–8

[28] Gao Y., Jakubowski M.W., Drewelow P., Pisano F., Puig Sitjes A., Niemann H., Ali A. and Cannas B. 2019 Methods for quantitative study of divertor heat loads on W7-X *Nucl. Fusion* **59** 066007

[29] Sunn Pedersen T. *et al* 2016 Confirmation of the topology of the Wendelstein 7-X magnetic field to better than 1:100000 *Nat. Commun.* **7** 13493

[30] Krychowiak M. *et al* 2021 Gaussian process tomography of carbon radiation in the transition to detached plasmas in the Wendelstein 7-X stellarator Proc. 47th EPS Conf. Plasma Physics

[31] Bozhenkov S.A., Geiger J., Grahl M., Kißlinger J., Werner A. and Wolf R.C. 2013 Service oriented architecture for scientific analysis at W7-X. An example of a field line tracer *Fusion Eng. Des.* **88** 2997–3006

[32] Barbui T. *et al* (W7-X team) 2019 The He/Ne beam diagnostic for line-ratio spectroscopy in the island divertor of Wendelstein 7-X *J. Instrum.* **14** C07014

[33] Killer C. *et al* 2019 Effect of toroidal plasma currents on the Wendelstein 7-X scrape-off layer *Plasma Phys. Control. Fusion* **61** 125014

[34] Perseo V. *et al* 2021 Direct 2D measurements of parallel counter-streaming flows in the W7-X scrape-off-layer for attached and detached plasmas *Nucl. Fusion* (accepted)